Structural basis for effector recognition by an antibacterial type IV secretion system

Gabriel U. Oka[a], Diorge P. Souza[a,1], William Cenens[a], Bruno Y. Matsuyama[a], Marcus V. C. Cardoso[a,2], Luciana C. Oliveira[a,3], Filipe da Silva Lima[a,4], Iolanda M. Cuccovia[a], Cristiane R. Guzzo[a,b], Roberto K. Salinas[a], and Chuck S. Farah[a,5]

[a]Department of Biochemistry, Institute of Chemistry, University of São Paulo, São Paulo 05508-000, SP, Brazil; and [b]Department of Microbiology, Institute of Biomedical Sciences, University of São Paulo, São Paulo 05508-000, SP, Brazil

Edited by Patricia Zambryski, Department of Plant and Microbial Biology, University of California, Berkeley, CA; received July 13, 2021; accepted November 19, 2021

Many soil-, water-, and plant-associated bacterial species from the orders Xanthomonadales, Burkholderales, and Neisseriales carry a type IV secretion system (T4SS) specialized in translocating effector proteins into other gram-negative species, leading to target cell death. These effectors, known as X-Tfes, carry a carboxyl-terminal domain of ∼120 residues, termed XVIPCD, characterized by several conserved motifs and a glutamine-rich tail. Previous studies showed that the XVIPCD is required for interaction with the T4SS coupling protein VirD4 and for T4SS-dependent translocation. However, the structural basis of the XVIPCD–VirD4 interaction is unknown. Here, we show that the XVIPCD interacts with the central all-alpha domain of VirD4 ($VirD4_{AAD}$). We used solution NMR spectroscopy to solve the structure of the XVIPCD of $X\text{-}Tfe^{XAC2609}$ from *Xanthomonas citri* and to map its interaction surface with $VirD4_{AAD}$. Isothermal titration calorimetry and in vivo *Xanthomonas citri* versus *Escherichia coli* competition assays using wild-type and mutant $X\text{-}Tfe^{XAC2609}$ and $X\text{-}Tfe^{XAC3634}$ indicate that XVIPCDs can be divided into two regions with distinct functions: the well-folded N-terminal region contains specific conserved motifs that are responsible for interactions with $VirD4_{AAD}$, while both N- and carboxyl-terminal regions are required for effective X-Tfe translocation into the target cell. The conformational stability of the N-terminal region is reduced at and below pH 7.0, a property that may facilitate X-Tfe unfolding and translocation through the more acidic environment of the periplasm.

type IV secretion system | bacterial competition | type IV coupling protein | *Xanthomonas* | protein NMR

Type IV secretion systems (T4SSs) are evolutionarily versatile multiprotein complexes that translocate macromolecular effectors (proteins or nucleoprotein conjugates) into target cells. They have important roles in bacterial pathogenesis in animal (1–4) and plant (5, 6) hosts, plasmid conjugation (7, 8) and other horizontal gene transfer processes (9, 10), bacteriophage uptake (11, 12), and interspecies bacterial competition (13–16). While there is a large diversity in the number of different subunits, overall size, and complexity, most T4SSs share a conserved core architecture best exemplified by the canonical type A systems consisting of 12 subunits: VirB1–VirB11 and VirD4. Multiple copies of these subunits come together to build a nanomachine that spans the envelope of gram-negative bacteria (17, 18). The VirD4 ATPase, also called the type IV coupling protein (T4CP), recruits substrates for secretion and delivers them to the inner membrane complex made up of two more ATPases, VirB4 and VirB11, plus the integral proteins VirB3, VirB6, VirB8, and the N-terminal domain of VirB10. The outer membrane or core complex is composed of 14 copies each of VirB9, the small lipoprotein VirB7, and the carboxyl-terminal domain of VirB10, which forms a pore in the outer membrane. The external pilus is a polymer of VirB2 pilin subunits and the associated VirB5. Finally, VirB1 is a periplasmic lytic transglycosylase thought to be involved in peptidoglycan remodeling during T4SS biogenesis (19–21).

We have previously demonstrated that *Xanthomonas citri,* the phytopathogen that causes citrus canker in citrus plants, and the soil bacterium *Stenotrophomonas maltophilia*, a common opportunistic human pathogen, both carry a chromosomally encoded class A T4SS that mediates interspecies bacterial killing by transferring a mixture of antibacterial effector proteins into competitor cells (13–15, 22, 23). Homologous systems, termed X-T4SSs (for Xanthomonadales-like T4SSs), have been identified in many Xanthomonadales species from the *Xanthomonas*, *Stenotrophomonas*, *Pseudoxanthomonas*, *Luteimonas*, *Lysobacter*, *Thermomonas*, *Rhodanobacter*, *Dyella*, *Frateuria*, and *Luteibacter* genera of Gammaproteobacteria as well as a more limited number of

Significance

Type IV secretion systems (T4SSs) have been studied for more than 70 y because of their roles in mediating horizontal DNA transfer, responsible for the spread of antibiotic resistance, and the injection of virulence factors into animal and plant hosts. Another important function is the contact-dependent injection of toxic effectors into competing bacteria of different species during bacterial warfare. The present study reveals how T4SSs use a specific domain of the VirD4 coupling protein to recruit antibacterial toxins for secretion by recognizing conserved carboxyl-terminal secretion signal domains. The molecular structure of the secretion signal domain described in this work will serve as a model for thousands of homologs encountered in several hundred distinct bacterial species.

Author contributions: G.U.O., D.P.S., R.K.S., and C.S.F. designed research; G.U.O., D.P.S., W.C., B.Y.M., M.V.C.C., L.C.O., C.R.G., R.K.S., and C.S.F. performed research; I.M.C. contributed new reagents/analytic tools; G.U.O., D.P.S., W.C., B.Y.M., M.V.C.C., L.C.O., F.d.S.L., C.R.G., R.K.S., and C.S.F. analyzed data; and G.U.O., R.K.S., and C.S.F. wrote the paper.

The authors declare no competing interest.

This article is a PNAS Direct Submission.

[1]Present address: Division of Cell Biology, MRC Laboratory of Molecular Biology, Cambridge, CB20QH, United Kingdom.

[2]Present address: Department of Chemistry, Institute of Exact and Biological Sciences, Federal University of Ouro Preto, Ouro Preto, Brazil, CEP 35400-000.

[3]Present address: Nmx Research and Solutions Inc., Laval, Québec, Canada, H7V 5B7.

[4]Present address: Department of Fundamental Chemistry, Center for Exact and Natural Sciences, Federal University of Pernambuco, Recife, Pernambuco, Brazil, CEP 507540-560.

[5]To whom correspondence may be addressed. Email: chsfarah@iq.usp.br.

This article contains supporting information online at http://www.pnas.org/lookup/suppl/doi:10.1073/pnas.2112529119/-/DCSupplemental.

Published December 30, 2021.

Betaproteobacteria species (genera *Hydrogenophaga*, *Variovorax*, *Neisseria*, and *Morococcus*) (14). We have shown that the closely related *Xanthomonas citri* and *Stenotrophomonas maltophilia* can use their X-T4SSs to kill each other, as well as more distant gram-negative bacterial species of different classes (13, 15), thereby demonstrating the potentially important role of this secretion system for interspecies competition in a wide variety of niches. All these systems share features that distinguish them from other class A T4SSs, including larger VirB7 and VirB8 subunits and specific gene order within the chromosomally located *vir* locus (14, 24, 25).

Another feature shared by X-T4SSs is the cohort of secreted effectors, called X-Tfes (Xanthomonadales-like T4SS effectors), that present a large variety of N-terminal catalytic domains, responsible for their toxic activities, as well as a ∼120-residue carboxyl-terminal region, termed *Xanthomonas* VirD4 interacting protein conserved domain (XVIPCD) (13, 14, 25). The genes coding for these X-Tfes are always found in operons, paired with upstream genes that code for their cognate inhibitors, called Xanthomonadales-like T4SS immunity proteins (X-Tfis) (13, 15). The *X. citri* genome codes for 13 potential X-Tfes. Three of these (XAC0323, XAC3404, XAC1165) are very small proteins (127–136 residues) made up of only an XVIPCD, and two others (XAC4264, XAC0151) may be truncated or inactivated proteins because of deletions or frameshift mutations in their N-terminal domains (13, 14, 25). Of the remaining eight X-Tfes, seven carry N-terminal catalytic domains that potentially target glycosidic and/or peptide bonds in the peptidoglycan layer (XAC2609, XAC0466, XAC3634, XAC1918, XAC0096) or are predicted to have phospholipase activity (XAC0574, XAC2885), while the eighth, XAC3266, is a predicted nuclease (13, 14, 25).

X-Tfes are identifiable by the presence of their common XVIPCDs, which were first revealed through their common abilities to interact with VirD4 (25) and later shown to be absolutely required for the secretion of X-Tfes by *X. citri* (13) and *S. maltophilia* (15). XVIPCDs are characterized by an N-terminal region containing several conserved sequence motifs and a glutamine-rich carboxyl-terminal region (25), though the structural basis of their interaction with VirD4 is not known. In the present study, we solved the three-dimensional structure of the X-Tfe^{XAC2609} XVIPCD by solution NMR. We employed NMR, isothermal titration calorimetry (ITC), and in vivo bacteria-killing assays of X-Tfe^{XAC2609} and X-Tfe^{XAC3634} mutants to identify specific residues and structural features involved in the XVIPCD interaction with the central all-alpha domain (AAD) of VirD4 as well as those features required for subsequent secretion by the X-T4SS.

Results

X-Tfe XVIPCDs Interact with the VirD4 AAD. In VirD4 proteins from *Agrobacterium tumefaciens* and *Enterococcus faecalis* plasmid pCf10, the central alpha-helix–rich domain (called the AAD) has been shown to mediate interactions with substrate molecules (26). *SI Appendix*, Fig. S1 presents an alignment of the VirD4 proteins from *X. citri*, *A. tumefacens*, pCf10, and TrwB from the *Escherichia coli* plasmid R388, the last of which has had its structure determined (27). We have shown that full-length *X. citri* VirD4 interacts with the XVIPCD region of X-Tfes (25) and that the translocation of the X-Tfe coded by the *xac2609* gene (X-Tfe^{XAC2609}) is dependent on the presence of its XVIPCD (13). *SI Appendix*, Fig. S2 *A* and *B* show that when separate bacterial cell cultures expressing the X-Tfe^{XAC2609} XVIPCD (XAC2609$_{XVIPCD}$) and the *X. citri* VirD4 AAD (VirD4$_{AAD}$) carrying a His-tag (VirD4$_{HIS\text{-}AAD}$) are combined and lysed together, a stable XAC2609$_{XVIPCD}$-VirD4$_{HIS\text{-}AAD}$ complex is obtained by affinity purification. Similar results are obtained when a complete VirD4 cytosolic fragment (VirD4$_{83–557}$) is coexpressed with XAC2609$_{XVIPCD}$ carrying an N-terminal His-tag (*SI Appendix*, Fig. S3). Size-exclusion chromatography (SEC) coupled to multiangle light scattering (MALS) analyses of purified VirD4$_{AAD}$ and XAC2609$_{XVIPCD}$ on their own and when mixed at a 1:1 ratio show that both isolated polypeptides are monomers and that they can form a stable 1:1 complex at pH 7.0 and 8.0, but the complex is destabilized as the pH is lowered to 6.0 and 4.5 (Fig. 1*A*; *SI Appendix*, Fig. S2*C* and Table S1). XAC2609$_{XVIPCD}$ at pH 8.0 presents a small-angle X-ray scattering (SAXS) Kratky plot characteristic of partially unfolded proteins (Fig. 1*B*) (28). SAXS analysis of VirD4$_{AAD}$ and the VirD4$_{AAD}$–XAC2609$_{XVIPCD}$ complex, on the other hand, reveals that they are predominantly folded and globular in solution (Fig. 1*B*), suggesting that XAC2609$_{XVIPCD}$ folds, at least partially, upon interaction with VirD4$_{AAD}$. We then used *X. citri* VirD4$_{AAD}$ as a bait in yeast two hybrid assays against a library of proteins and protein fragments coded by the *X. citri* genome (29). Nine preys derived from four different proteins (XAC0151, XAC0096, XAC3266, XAC2885) were isolated (Table S2), all of which had been previously identified as X-Tfes (13, 25). The previous observations all confirm that the XVIPCDs of different X-Tfes interact with the VirD4$_{AAD}$. We therefore decided to investigate the structural basis of the interaction of XAC2609$_{XVIPCD}$ with VirD4$_{AAD}$ in more detail.

The Glutamine-Rich Carboxyl-Terminal Tails of XVIPCDs Present Regions with Conserved Physicochemical Properties but Are Not Required for Interaction with the VirD4 AAD. X-Tfes with characteristic XVIPCDs have been identified in a large number of proteobacterial species concentrated in the Xanthomonadales, Burkholderiales, and Neisseriales orders (13, 14). Fig. 2 *A* and *B* present the amino acid conservation profile of an alignment of 4756 XVIPCD sequences identified in the protein sequence databases in more than 350 different bacterial species and strains (Table S4). The alignment is divided into two parts: i) The N-terminal ααββββ region (see the section titled *NMR structure of XAC2609$_{XVIPCD}$Δ20* below) has the most well-conserved positions corresponding to His315, Gly336, Asp363, His364, Val365, Phe375, Val377, Gln378, Gly379, Pro384, Arg388, Ala396, Pro400, and Ser404 in X-Tfe^{XAC2609} (Fig. 2*A*; Dataset S1), while ii) after the position corresponding to Ser404, we observe a large divergence in both sequence and length of what we will now call the XVIPCD carboxyl-terminal tail. Fig. 2*B* shows the size distribution of carboxyl-terminal tails in the XVIPCD dataset counting from the position corresponding to Ser404 in X-Tfe^{XAC2609}. The length varies from 2 to 88 residues, with the maximum of the distribution at 34 residues (12% of sequences) and 90% of the sequences falling within the range of 26–42 residues (Fig. 2*B*; Dataset S2).

Since the results we will present below (see section titled *XVIPCD Features Required for Secretion of X-Tfe^{XAC2609}*) and studies on other T4SS substrates have pointed to the contribution of their carboxyl termini as secretion recognition signals, we analyzed the chemical properties of the carboxyl-terminal tails in the XVIPCD dataset (Fig. 2*B*). This analysis shows that they can be divided into an N-terminal region, from the conserved serine to position −8 counting from the carboxyl terminus, that is rich in glutamine, alanine, and charged residues (usually glutamate and arginine), while the extreme carboxyl-terminal region (positions −6 to −1) carries one or more arginines, lacks negatively charged residues, and is enriched in both hydrophobic (Met, Pro, and Leu) and/or small volume residues (Ala, Gly, and Ser).

In the case of X-Tfe^{XAC2609}, the last 20 residues of the carboxyl-terminal tail contain five glutamine residues as well as six serines or threonines, two arginines, and one glutamate (Fig. 2*C*). To study the importance of the XVIPCD carboxyl-terminal tail, we cloned, expressed, and purified a XAC2609$_{XVIPCD}$ construction lacking

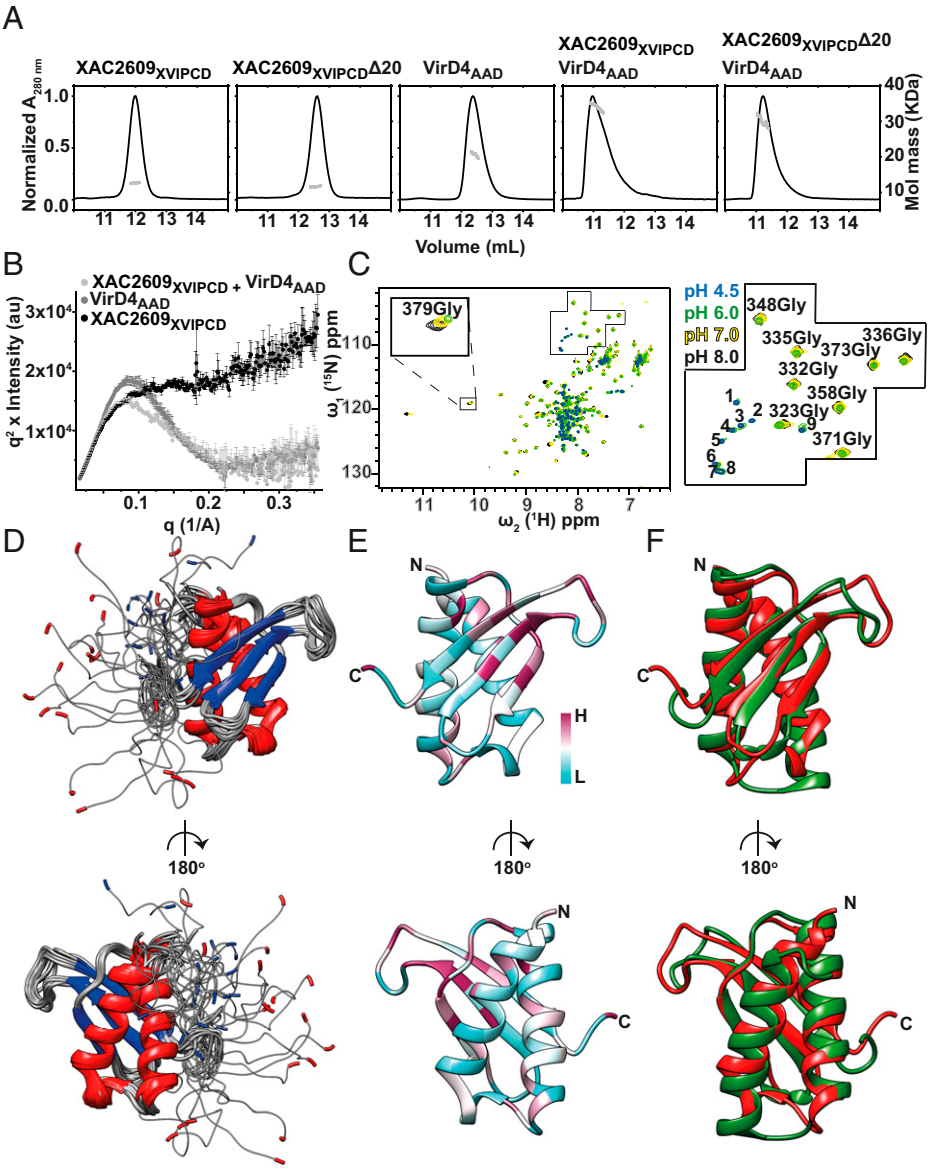

Fig. 1. Complex formation between the VirD4$_{AAD}$ domain and XAC2609$_{XVIPCD}$. (*A*) SEC-MALS analysis of purified recombinant XAC2609$_{XVIPCD}$, XAC2609$_{XVIPCD}$Δ20, VirD4$_{AAD}$, and purified VirD4$_{AAD}$–XAC2609$_{XVIPCD}$ and VirD4$_{AAD}$–XAC2609$_{XVIPCD}$Δ20 complexes at pH 8.0 (20 mM Tris·HCl, 200 mM NaCl, 2% glycerol). Normalized absorbances at 280 nm (black lines, left axis) and molecular mass distributions (gray dots, right axis) are plotted as a function of elution volume. (*B*) SAXS Kratky plot [I(q)$_x$q^2 versus q] of XAC2609$_{XVIPCD}$ (black), VirD4$_{AAD}$ (dark gray), and the VirD4$_{AAD}$–XAC2609$_{XVIPCD}$ complex (light gray). X-ray scattering intensity (I(q)) is in arbitrary units (au), and the scattering vector (q) is shown in Å^{-1}. Curves are the mean of two or three independent assays; error bars represent the SD. (*C*) Superposition of ^{15}N-^{1}H HSQC spectra of ^{15}N-labeled XAC2609$_{XVIPCD}$Δ20 at different pHs: 4.5 (blue), 6.0 (green), 7.0 (yellow), and 8.0 (black). *Inset* shows the region containing cross-peaks of glycine residues. (*D*) Ribbon representation of the ensemble of the 20 lowest-energy NMR structures of XAC2609$_{XVIPCD}$Δ20 (residues 311–411). Highly flexible N- and carboxyl-terminal regions (residues 311–314 and 397–411) are shown as narrow ribbons. (*E*) The lowest-energy NMR model of the well-folded αααβββ region (residues 315–396) colored according to degree of conservation (lowest, cyan; highest, purple) within the XVIPCD superfamily (see Fig. 2*A*). (*F*) Superposition of the XAC2609$_{XVIPCD}$Δ20 NMR model (red) and the predicted XAC2609$_{XVIPCD}$Δ20 structure generated by the RaptorX server (green) that uses evolutionary coupling and sequence conservation information to predict contacts between pairs of residues in a family of related proteins (36, 37).

these last 20 residues (XAC2609$_{XVIPCD}$Δ20). SEC-MALS analysis shows that this 11.5 kDa fragment is a monomer and is still able to form a 1:1 heterodimeric complex with VirD4$_{AAD}$ (Fig. 1*A*; *SI Appendix*, Fig. S2*C* and Table S1). *SI Appendix*, Fig. S4*B* compares the ^{1}H-^{15}N heteronuclear single quantum coherence (HSQC) NMR spectra of XAC2609$_{XVIPCD}$ (residues 311–431) and XAC2609$_{XVIPCD}$Δ20 (residues 311–411) at 25 °C and pH 8.0. We observe that the shorter XAC2609$_{XVIPCD}$Δ20 polypeptide presents a greater number of cross-peaks than the full-length domain, suggestive of a more folded and well-ordered structure. Based on the previous considerations, we chose to employ XAC2609$_{XVIPCD}$Δ20 in subsequent NMR studies aimed at determining its structure in solution.

The XVIPCD Is Partially Unfolded at Neutral and Slightly Acidic pH. Interestingly, the ^{1}H-^{15}N HSQC spectrum of XAC2609$_{XVIPCD}$Δ20 collected at pH 4.5 presents 125 cross-peaks (124 expected), similar to the number observed at pH 8.0 (119 peaks) but with a much narrower chemical shift range (Fig. 1*C*; *SI Appendix*, Fig. S4*A*). This suggests a less-ordered three-dimensional structure at low

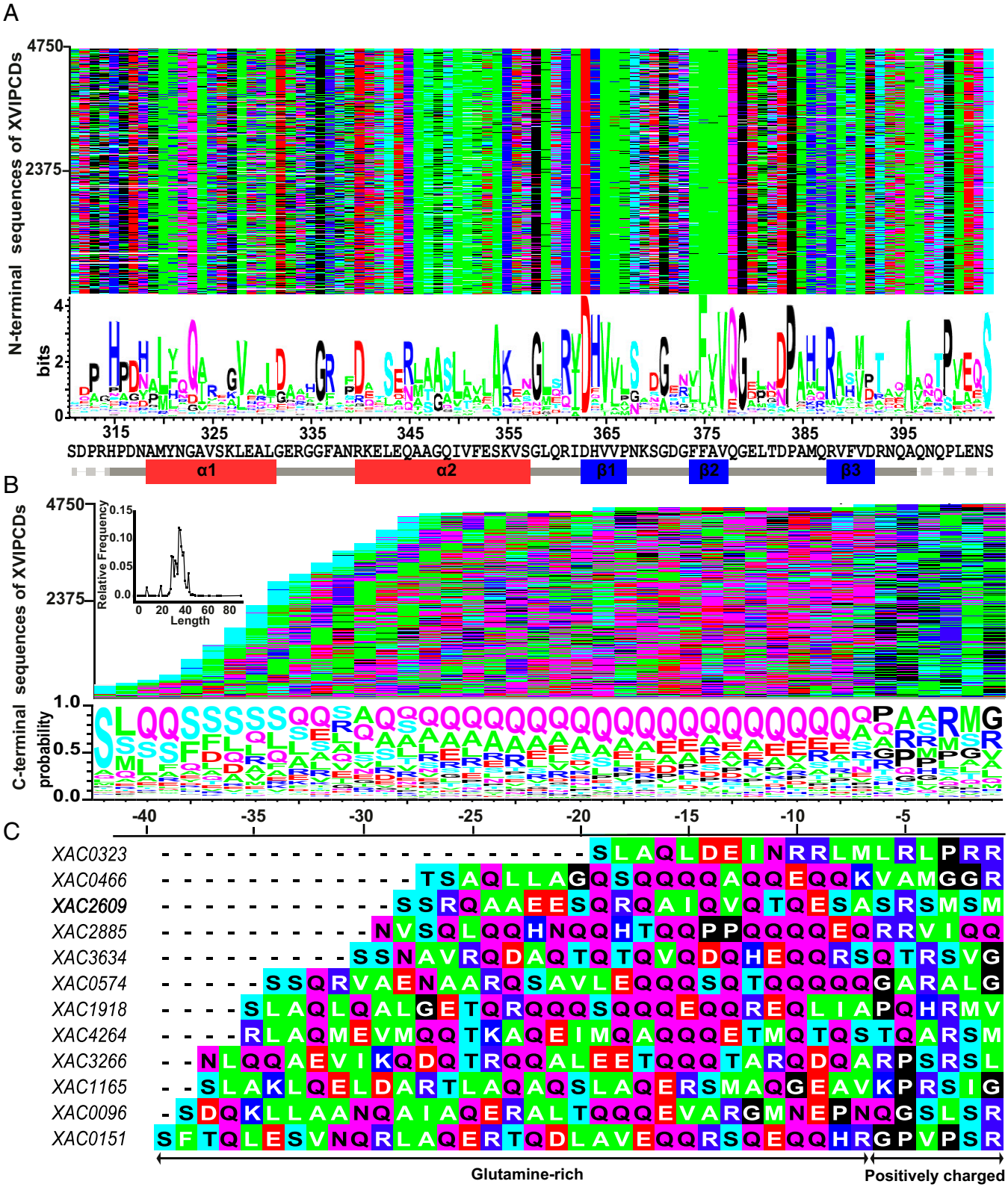

Fig. 2. The XVIPCD superfamily. (*A*) Sequence alignment (*Top*) and sequence conservation profile (*Bottom*) of the XVIPCD N-terminal ααβββ region, derived from 4,750 nonidentical sequences obtained from the nonredundant National Center for Biotechnology Information (NCBI) protein database (72). The conservation profile is aligned to the X-Tfe^{XAC2609} XVIPCD sequence (residues 315–404), with insertions removed. Residues are colored as follows: S, T (cyan); E, D (red); Q, N (purple); R, K, H (blue); A, F, L, M, I, V, W, Y (green); C, G, P (black); and gaps due to deletions with respect to X-Tfe^{XAC2609} (white). Secondary structure elements in the XAC2609$_{XVIPCD}$Δ20 structure are shown: α-helices (red rectangles), β-strands (blue rectangles), loops (gray lines), and nonassigned regions (dotted gray lines). The complete alignment is provided in Dataset S1. (*B*) Alignment of the carboxyl-terminal tail portions of members of the XVIPCD superfamily. Here, sequences were ordered according to their length starting from the last highly conserved position in the XVIPCD superfamily, corresponding to Ser404 in X-Tfe^{XAC2609}, and aligned with respect to their carboxyl-terminal residues, considered here as position −1. Residues are colored as in *A*. The inset presents the relative frequencies of the lengths of carboxyl-terminal tails in the XVIPCD superfamily. The complete alignment is provided in Dataset S2. (*C*) Sequences of the carboxyl-terminal tails of *X. citri* X-Tfe XVIPCDs.

pH. However, at intermediate pH values, the number of cross-peaks increases substantially to 212 at pH 6.0 and 200 at pH 7.0 (Fig. 1*C*; *SI Appendix*, Fig. S4*A*). Superposition of the ^{1}H-^{15}N HSQC spectra collected at pH 4.5, 6.0, 7.0, and 8.0 suggests that data acquired at pH 6.0 and 7.0 can be interpreted as linear combinations of the spectra collected at pH 4.5 and 8.0 (Fig. 1*C*). These observations suggest that at neutral and slightly acidic pH, $XAC2609_{XVIPCD}\Delta20$ undergoes a slow exchange between folded and partially unfolded states. This conclusion is supported by the observation that as the pH is lowered from 8.0 to 7.0, 6.0, and 4.5, both $XAC2609_{XVIPCD}$ and $XAC2609_{XVIPCD}\Delta20$ remain monomeric while migrating through SEC columns with apparently larger hydrodynamic radii (*SI Appendix*, Fig. S2 and Table S1).

In order to determine whether this pH-dependent conformational instability is a characteristic of only the XVIPCD domain or extends to other regions of the X-Tfe^{XAC2609} protein, we used circular dichroism to perform thermal denaturation assays on $XAC2609_{XVIPCD}$, full-length X-Tfe^{XAC2609}, and its N-terminal fragment (X-Tfe$^{XAC2609}{}_{1–306}$) lacking the XVIPCD at pH 8.0 and pH 5.0. *SI Appendix*, Fig. S5 shows that all three polypeptides present significant secondary structure at pH 8.0 and clear thermal denaturation isotherms. At pH 5, however, the full-length protein and its N-terminal fragment present significant secondary structure and denaturation isotherms with transition midpoint temperatures very similar to those observed at pH 8.0 (all between 35 and 40 °C). On the other hand, the XVIPCD fragment at pH 5.0 presents a circular dichroism (CD) spectrum characteristic of a random-coil polypeptide at room temperature, and no significant change in CD signal is observed as the temperature is raised. Furthermore, at both pH values, the raw denaturation isotherm of the full-length protein is very similar to the sum of denaturation isotherms of the N-terminal and C-terminal fragments (*SI Appendix*, Fig. S5*C*). These pH-dependent conformational transitions in the XVIPCD could be physiologically relevant as X-T4SS substrates are translocated through the periplasm, where the pH, determined in part by the external environment, may be significantly lower than in the bacterial cytosol (cytosolic pH in *E. coli* is estimated to be between 7.6 and 7.8; refs. 30–32).

NMR Structure of $XAC2609_{XVIPCD}\Delta20$. The $XAC2609_{XVIPCD}\Delta20$ backbone and side-chain (^{1}H, ^{15}N, and ^{13}C) resonances were assigned (*SI Appendix*, Fig. S6) and 2,383 NMR distance and 154 dihedral angle restraints were used to calculate a family of the 20 lowest-energy structures at pH 8.0 (Fig. 1*D*). Data collection and structural refinement statistics are presented in Table S3. The $XAC2609_{XVIPCD}\Delta20$ structure presents two well-ordered N-terminal antiparallel alpha-helices (α1 and α2; residues 316–331 and 340–357, respectively) that pack against a carboxyl-terminal three-stranded antiparallel beta sheet (β1, β2, β3; residues 363–367, 373–378, and 387–392, respectively). Analysis of chemical shifts using the TALOS-N algorithm (33) showed that these five secondary structure elements all have high random coil index (RCI) order parameters, while the amino and carboxy-terminal regions of $XAC2609_{XVIPCD}\Delta20$ (residues 311–318 and 393–411, respectively) are conformationally heterogeneous, which is consistent with the observation of {^{1}H}-^{15}N heteronuclear nuclear Overhauser effects (NOEs) lower than 0.8 at the carboxyl and the N termini (Fig. 1*D*; *SI Appendix*, Fig. S4*C*). Resonances of 8 of last 19 residues from the carboxyl terminus of $XAC2609_{XVIPCD}\Delta20$ (residues 397–399 and 403–407) could not be identified during backbone assignment, while the side-chain atoms of the remaining 11 residues were only partially assigned. The only medium- or long-range NOEs observed for this region involve Pro400 with the side chains of Asp372, Phe390, Asp392, Arg393, and Asn394 (*SI Appendix*, Fig. S4*D*). We note that residues Ala396, Pro400, and Ser404 within this region that links the ααβββ region with the carboxyl-terminal tail are among the most well-conserved positions in the XVIPCD alignment (Fig. 2*A*).

XVIPCD sequences are not similar to any other protein families with known structures (see *SI Appendix*, Supplementary Text; refs. 34, 35). We therefore asked whether the alignment of the large number of XVIPCD sequences could be used to identify coevolution of residue pairs and predict contacts in the three-dimensional structures of members of this superfamily. For this, we employed the RaptorX server (http://raptorx.uchicago.edu/) (36, 37). Fig. 1*F* shows that the model predicted by RaptorX is strikingly similar (rmsd of 2.0-Å Cα atoms of residues 315–396) and has the same topology as the $XAC2609_{XVIPCD}\Delta20$ NMR structure, with the most significant deviations in the flexible loops connecting secondary structure elements. The success of RaptorX in predicting the fold of the XVIPCD is an independent validation of the experimentally determined $XAC2609_{XVIPCD}\Delta20$ NMR structure, and similar results were obtained using inputs of XVIPCD sequences from all other X-Tfes tested (examples of RaptorX predictions for XVIPCDs from nine taxonomic genera are shown in *SI Appendix*, Fig. S7).

XVIPCD Features Required for Interaction with $VirD4_{AAD}$. We next carried out a set of experiments to determine in more detail which features of the well-folded N-terminal ααβββ domain and conformationally flexible, less-conserved carboxyl-terminal tail are required for interaction with VirD4 and/or subsequent translocation by the X-T4SS into the target cell. Fig. 3*A* shows the ^{15}N-^{1}H HSQC spectrum of ^{15}N-labeled $XAC2609_{XVIPCD}\Delta20$ on its own (black) and in the presence of a stoichiometric excess (2:1) of unlabeled $VirD4_{AAD}$ (red), which induces a large set of chemical shift perturbations. The changes in the spectra at intermediate $VirD4_{AAD}$:$XVIPCD_{XAC2609}\Delta20$ ratios are consistent with slow exchange on the NMR time scale (titration points are shown in *SI Appendix*, Fig. S8). In the absence of definitive assignments for the backbone of $XAC2609_{XVIPCD}\Delta20$ in complex with $VirD4_{AAD}$, we quantified the changes in the spectra in two different manners. Firstly, we measured the ratios of the peak heights in the ^{15}N-^{1}H HSQC spectra collected in the presence versus absence of unlabeled $VirD4_{AAD}$ at the frequencies of the centers of the ^{15}N-^{1}H cross-peaks for the 79 assigned $XAC2609_{XVIPCD}\Delta20$ backbone amides in the absence of $VirD4_{AAD}$ (Fig. 3*B*, black bars). Here, in addition to cross-peak broadening due to increased correlation times, any shift in cross-peak position upon addition of $VirD4_{AAD}$ will result in a reduced intensity ratio. Secondly, in many cases, very moderate frequency shifts were observed, which allowed us to tentatively assign a fraction of the cross-peaks in the spectrum of the $XAC2609_{XVIPCD}\Delta20$–$VirD4_{AAD}$ complex. In these cases, we measured the ratio of the heights at the cross-peak centers in both the presence and absence of $VirD4_{AAD}$ (Fig. 3*B*, gray bars). For the remaining residues, the addition of $VirD4_{AAD}$ either caused the cross-peak to broaden so much as to be undetectable or its chemical shift was perturbed so much as to create an ambiguity in its assignment (in these ambiguous cases, the gray bars repeat the zero or near-zero values of the black bars). The residues whose resonances suffered significant (>90%) reductions in ^{1}H-^{15}N cross-peak height can be considered strong candidates for participating in the interaction with $VirD4_{AAD}$ and are mapped on the $XAC2609_{XVIPCD}\Delta20$ structure in Fig. 3*C* (red to yellow scale), in which it can be seen that they cluster mainly on the surface of the three-stranded beta sheet and its associated loops with a few residues in the hydrophobic core of the protein also showing perturbations. Comparison of Figs. 1*E*, 2*A*, and 3*C* shows a good correlation between the most highly conserved residues and those with the most significant $VirD4_{AAD}$-induced perturbations in the ^{1}H-^{15}N-HSQC spectrum.

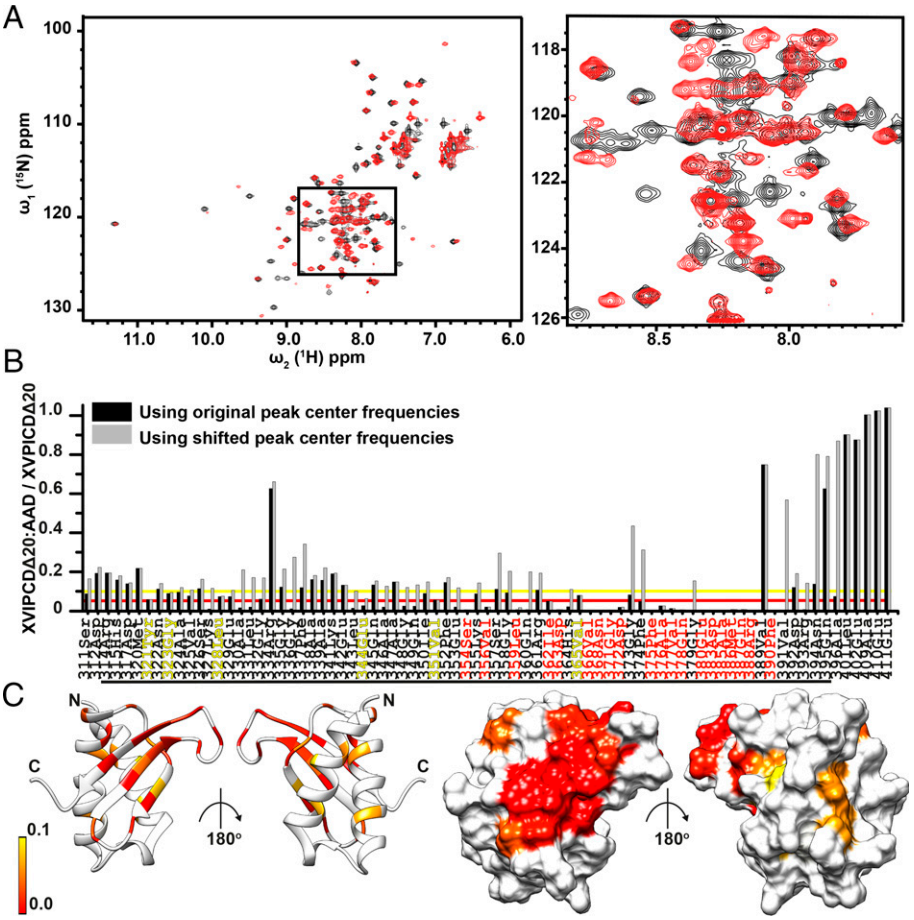

Fig. 3. Mapping of the VirD4$_{AAD}$ binding site on XAC2609$_{XVIPCD}$Δ20. (*A*) Superposition of ^{15}N-^{1}H HSQC spectra of ^{15}N-labeled XAC2609$_{XVIPCD}$Δ20 (160 μM) on its own (black) and in the presence of a twofold excess of unlabeled VirD4$_{AAD}$ (red). XAC2609$_{XVIPCD}$Δ20 ^{15}N-^{1}H cross-peak assignments are indicated. (*B*) Quantification of changes induced in the ^{15}N-^{1}H HSQC spectrum of ^{15}N-labeled XAC2609$_{XVIPCD}$Δ20 by addition of unlabeled VirD4$_{AAD}$. Two methods of quantification are shown. Black bars show the ratio of peak heights observed in the presence versus the absence of VirD4$_{AAD}$, both measured at the center of the 79 backbone amide cross-peaks observed in the absence of VirD4$_{AAD}$. Here, in addition to cross-peak broadening due to increased correlation times, shifts in cross-peak position upon addition of VirD4$_{AAD}$ will result in a reduced intensity ratio. Cross-peaks that underwent only very moderate or no frequency shifts upon addition of VirD4$_{AAD}$ were tentatively assigned in the spectrum of the XAC2609$_{XVIPCD}$Δ20–VirD4$_{AAD}$ complex. Gray bars show the peak height ratio measured at the centers of the XAC2609$_{XVIPCD}$Δ20 cross-peaks in the presence of VirD4$_{AAD}$ versus the peak height measured at the center of the cross-peak in the absence of VirD4$_{AAD}$. Residues whose black and gray bars are both below 0.05 or 0.1 are colored red or yellow, respectively. Red and yellow horizontal lines are drawn at peak height ratios of 0.05 and 0.1, respectively. (*C*) Cartoon (*Left*) and surface (*Right*) representation of the XAC2609$_{XVIPCD}$Δ20 structure with residues with the greatest reductions in peak intensities upon addition of VirD4$_{AAD}$ colored on a scale from red (0) to yellow (0.1). Residues with peak intensity ratios above 0.1 are colored white.

We then investigated the effect of mutating specific XAC2609$_{XVIPCD}$ residues on the interaction with VirD4$_{AAD}$. We expressed and purified a set of XAC2609$_{XVIPCD}$ polypeptides in which one or more conserved residues in the ααββββ region were mutated. We also produced XAC2609$_{XVIPCD}$Q(397–431)A, in which all eight glutamine residues in the carboxyl-terminal tail of XAC2609$_{XVIPCD}$ (positions 397, 399, 407, 413, 415, 418, 420, 422) were simultaneously changed to alanine. In addition to the XAC2609$_{XVIPCD}$Δ20 deletion mutant, we also produced the XAC2609$_{XVIPCD}$Δ6 deletion mutant that lacks the last six residues (426–431) corresponding to the positively charged zone of the carboxyl-terminal tail. A fragment corresponding to the last 40 residues of the XVIPCD (XAC2609$_{392–431}$) was also produced. These XAC2609$_{XVIPCD}$ mutants were used along with XAC2609$_{XVIPCD}$ and full-length X-Tfe^{XAC2609} in ITC experiments to determine their dissociation constants with VirD4$_{AAD}$ (*SI Appendix*, Fig. S9 and Table S5). We observed that XAC2609$_{XVIPCD}$, the XAC2609$_{XVIPCD}$Δ20 and XAC2609$_{XVIPCD}$Δ6 deletion mutants, and XAC2609$_{XVIPCD}$Q(397–431)A all had only slightly greater dissociation constants (between 0.5 ± 0.1 μM and 0.6 ± 0.1 μM) than that observed for full-length X-Tfe^{XAC2609} (0.4 μM nM ± 0.1 μM) (Table S5). On the other hand, no interaction was observed for XAC2609$_{392–431}$ with VirD4$_{AAD}$ in ITC experiments (*SI Appendix*, Fig. S9*A*) or with VirD4$_{83–557}$ in pull-down experiments (*SI Appendix*, Fig. S3). These results are all consistent with the idea that the carboxyl-terminal tail contributes very little or not at all to the interaction with VirD4$_{AAD}$. Finally, since some T4CPs have carboxyl-terminal extensions that they use to interact with substrates (38–40), we produced an *X. citri* VirD4 fragment corresponding to residues 487–557. *SI Appendix*, Fig. S9*A* shows that no significant interaction was detected between VirD4$_{487–557}$ and XAC2609$_{XVIPCD}$ in ITC experiments.

Turning our attention to conserved residues in the ααββββ region, the point mutations G336W and A396M also only produced very moderate increases in K_D values (0.5 ± 0.3 μM and 0.7 ± 0.3 μM, respectively). Two other mutants produced more significant increases in K_D values: P400A (0.9 ± 0.6 μM) and H315A/P316A/D317A (1.2 ± 0.1 μM). Finally, the three mutants that caused the greatest decrease in affinity (55-fold or greater increases in K_D values) were D383/P384A (28 ± 25

μM), D363A (29 ± 7 μM), and F375A/V377A, for which no interaction could be detected (*SI Appendix*, Fig. S9 and Table S5). Phe375 and Val377 are both surface-exposed hydrophobic residues in the central strand (β2) of the β-sheet and are in close proximity to the surface-exposed Asp363 at the N terminus of β1, and Asp383 and Pro384 are located in the loop between β2 and β3 (*SI Appendix*, Fig. S9*B*). The backbone amides of Asp363, Phe375, Val377, and Asp383 all underwent significant chemical shift perturbations induced by $VirD4_{AAD}$ binding (Fig. 3*B*). Furthermore, in pull-down experiments using the His-tagged $XAC2609_{XVIPCD}$F375A/V377A mutant, no interaction with $VirD4_{AAD}$ (*SI Appendix*, Fig. S10) or with $VirD4_{83–557}$ (*SI Appendix*, Fig. S3) was observed. Taken together, the NMR, calorimetry, and pull-down experiments point to the beta sheet of $XAC2609_{XVIPCD}$ as the principal structural feature involved in its interaction with $VirD4_{AAD}$ and that this interaction involves both exposed hydrophobic (Phe375, Val377) and negatively charged (Asp363 and Asp383) residues that are relatively well conserved in the XVIPCD superfamily (Fig. 2*A*). Finally, no interaction was observed in ITC experiments (*SI Appendix*, Fig. S9*C*) and pull-down experiments (*SI Appendix*, Fig. S10) between the *X. citri* $VirD4_{AAD}$ and T4SS substrates PcfF and PcfG from *E. faecalis* and VirD2 from *A. tumefaciens*.

XVIPCD Features Required for Secretion of X-Tfe^{XAC2609}. We have previously shown that the XVIPCD region of X-$Tfe^{XAC2609}$ is required for its X-T4SS–dependent transfer into target cells (13). In order to determine which specific XVIPCD structural features are required for transfer, we employed the *X. citri* Δ7Δ2609-GFP strain in which seven X-Tfe/X-Tfi effector/immunity protein pairs (XAC2885/XAC2884, XAC0574/XAC0573, XAC0096/XAC0097, XAC3634/XAC3633, XAC1918/XAC1917, XAC0466/XAC0467, XAC4264/XAC4263/XAC4262) were deleted and the gene for X-$Tfe^{XAC2609}$ was exchanged with the gene for superfolder GFP. The Δ7Δ2609-GFP strain therefore lacks eight X-Tfe genes predicted to target the peptidoglycan or lipid bilayer in the target cell envelope. When equal numbers of *X. citri* and *E. coli* are mixed and grown as a coculture on agar plates, 14 times more wild-type *X. citri* cells are recovered than *E. coli*, while the Δ7Δ2609-GFP:*E. coli* ratio (0.008) is ∼3 orders of magnitude less, similar to that observed for *X. citri* with a nonfunctional X-T4SS (Δ*virB7*). Competitiveness is significantly recovered when the Δ7Δ2609-GFP strain is transformed with a plasmid expressing X-$Tfe^{XAC2609}$ (*X. citri*:*E. coli* = 0.23; Fig. 4*A*). Time-lapse fluorescence microscopy experiments show that while the Δ7Δ2609-GFP strain is not able to induce contact-dependent lysis of target *E. coli* RFP cells (Fig. 4*B*; Movie S1), killing activity is recovered by the complemented Δ7Δ2609-GFP + X-$Tfe^{XAC2609}$ strain (Fig. 4*B*; Movie S2). Moreover, Movie S2 shows that *X. citri* Δ7Δ2609-GFP complemented with X-$Tfe^{XAC2609}$ frequently induces spheroplasts in target *E. coli* cells before their eventual lysis. These results demonstrate that in the absence of seven other X-Tfes, the secretion of X-$Tfe^{XAC2609}$ by the X-T4SS confers an advantage to *X. citri* cells grown in coculture with *E. coli.* Similar results have been obtained using the X-$Tfe^{Smlt3024}$ toxin from *S. maltophilia* secreted by the related Δ8Δ2609-GFP *X. citri* strain (15).

To correlate the effect of a mutation in the XVIPCD on the efficiency of X-$Tfe^{XAC2609}$ transfer, we transformed *X. citri* Δ7Δ2609-GFP with plasmids directing the expression of X-$Tfe^{XAC2609}$ with mutations in the XVIPCD and used these strains in chlorophenol red β-D-galactopyranoside (CPRG)-based colorimetric assays to quantitatively monitor real-time killing of *E. coli* cells (22, 23). Fig. 4*C* and *SI Appendix*, Fig. S11 show the time-dependent hydrolysis of the CPRG reagent by beta-galactosidase released from lysed *E. coli* cells, Fig. 4*D* presents the instantaneous slopes (first derivatives) of these curves, and Fig. 4*E* presents histograms of the maximum slope for each *X. citri* strain tested. The maximum slopes can be interpreted as a measure of the killing efficiency of that particular strain. Under the conditions tested, *X. citri* Δ7Δ2609-GFP expressing wild-type X-$Tfe^{XAC2609}$ kills with an efficiency ∼90% of that of *X. citri* wild-type cells. On the other hand, *X. citri* with a nonfunctional X-T4SS (Δ*virB7*), Δ7Δ2609-GFP carrying an empty vector, and Δ7Δ2609-GFP expressing X-$Tfe^{XAC2609}{}_{1–306}$ that lacks the XVIPCD do not induce *E. coli* lysis, as expected (Fig. 4 *C–E*). The X-$Tfe^{XAC2609}$ G336W, A396M, and P400A mutations do not significantly compromise *E. coli* killing, while H315A/P316A/D317A, D363A, and D383A/P384A mutations result in partial reductions in killing (48, 28, and 54% of wild-type levels, respectively; Fig. 4 *C–E*). Interestingly, the F375A/V377A double mutant of two surface-exposed residues important for binding to $VirD4_{AAD}$ drastically reduced *E. coli* killing (<5% with respect to wild type).

We then turned our attention to the glutamine-rich carboxyl-terminal tail of the XVIPCD of X-$Tfe^{XAC2609}$. Interestingly, changing the last eight glutamines to alanines only resulted in a slight reduction in killing activity (92% of wild-type levels), while deletion of the last 20 residues (X-$Tfe^{XAC2609(Δ20)}$) abolishes *E. coli* killing (Fig. 4 *C–E*). We note that in addition to being rich in glutamines, the large majority of XVIPCDs have a positively charged residue (most often arginine), one or more hydrophobic residues, and very often a serine residue within the last few positions of the carboxyl-terminal tail: the last six residues of X-$Tfe^{XAC2609}$ are SRSMSM (residues 426–431; Fig. 2*B*). Fig. 4 *C–E* and *SI Appendix*, Fig. S11 shows that deletion of the last six residues drastically reduces killing to 5% of wild-type levels, while the simple R427A mutation does not reduce *E. coli* killing.

In summary, all of the mutations that significantly impaired $XVIPCD_{XAC2609}Δ20$ binding to $VirD4_{AAD}$ also compromised the ability of X-$Tfe^{XAC2609}$ to be transferred into and lyse target *E. coli* cells, as could be expected. Of particular interest is the six-residue deletion in the carboxyl-terminal tail that impaired *E. coli* killing even though it did not significantly affect binding to $VirD4_{AAD}$. Thus, the extreme carboxyl terminus of the XVIPCD is apparently involved in an essential step in the secretion pathway that may be distinct from binding to $VirD4_{AAD}$.

XVIPCD Features Required for Secretion of X-Tfe^{XAC3634}. As mentioned in the introduction above, *X. citri* codes for five X-Tfes with N-terminal domains that potentially target the peptidoglycan layer. Three of these, X-$Tfe^{XAC2609}$, X-$Tfe^{XAC0466}$, and X-$Tfe^{XAC3634}$, have additional peptidoglycan-binding domains (Pfam accession PF01471), and the first two have been shown to hydrolyze *Micrococcus luteus* peptidoglycan in vitro because of the presence of N-terminal GH19 domains (Pfam accession PF00182) with predicted lysozyme activity (13, 14). X-$Tfe^{XAC3634}$ has an N-terminal soluble lytic transglycosylase domain (Conserved Domain Database accession cd00254) (41) with a conserved glutamate residue at position 35 predicted to participate in catalysis (Fig. 5*A*) (42, 43). Fig. 5*B* shows that purified recombinant X-$Tfe^{XAC3634}$ is indeed able to cleave *M. luteus* peptidoglycan in vitro and that the E35Q mutation abolishes this activity. Furthermore, the addition of the purified soluble recombinant X-$Tfi^{XAC3633}$ (lacking the N-terminal signal peptide and lipobox), predicted to be the cognate immunity protein of X-$Tfe^{XAC3634}$ (13), inhibits the in vitro peptidoglycan hydrolase activity of the effector (Fig. 5*B*). Fig. 5*C* shows that Δ7Δ2609-GFP cells carrying a plasmid that directs the expression of the X-$Tfe^{XAC3634}$–X-$Tfi^{XAC3633}$ pair increases the *X. citri*:*E. coli* ratio in cocultures by two orders of magnitude, and Fig. 5*D* and Movie S3 show time-lapse fluorescence microscopy

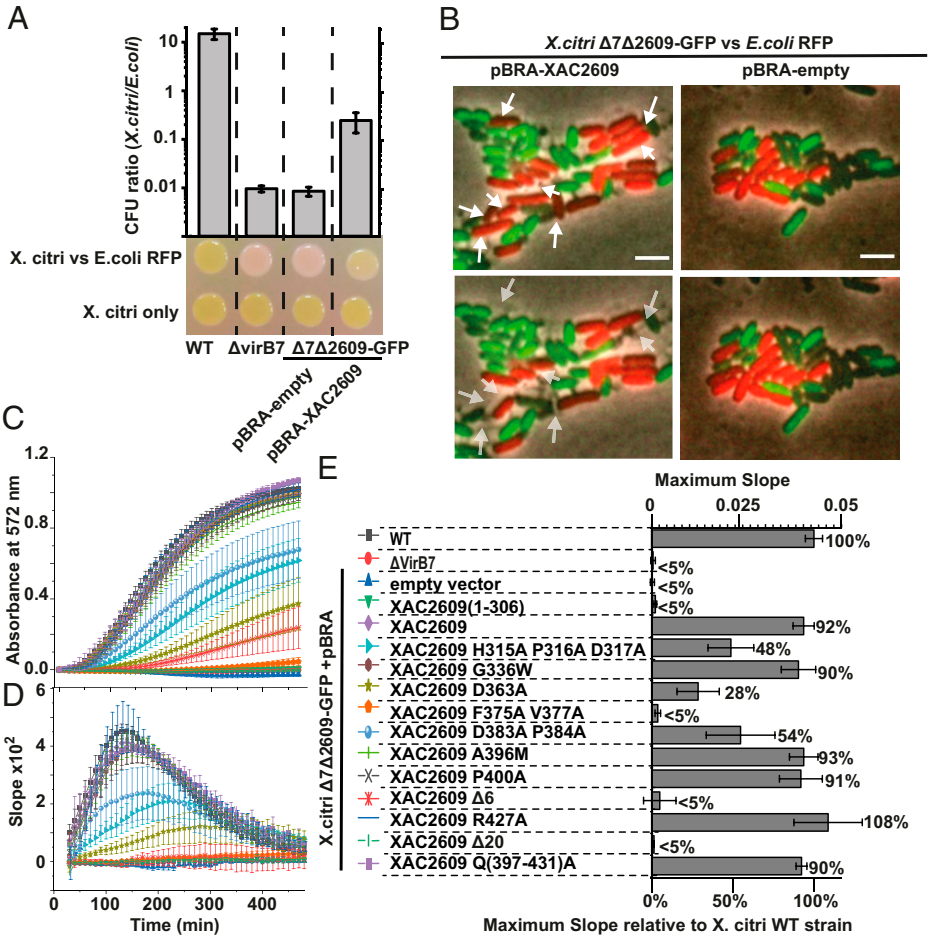

Fig. 4. XVIPCD features required for X-Tfe^{XAC2609} secretion. (*A*) The ratio of the number of viable *X. citri* and *E. coli* RFP cells after 36 h of interbacterial competition during coculture on Luria-Bertani (LB) agar. *X. citri* strains used: wild type (WT), Δ*vir*B7 (ΔVirB7), and Δ7ΔXAC2609-GFP carrying the empty pBRA vector or the pBRAXAC2609 vector expressing X-Tfe^{XAC2609}. Error bars represent the SD of three experiments. A representative image from a 36-h coculture assay is shown. (*B*) Time-lapse fluorescence microscopy showing *E. coli* expressing RFP (red) in coculture with *X. citri* Δ7ΔXAC2609-GFP (green) carrying the pBRA empty vector (*Right*) or pBRAXAC2609 (*Left*) at time points 0 min (*Top*) and after 20 min of incubation (*Bottom*). White and semitransparent arrows point to *E. coli* cells that underwent lysis during this 20-min interval. (Scale bar, 3 μm.) Movies S1 and S2 present time-lapse videos over more extended periods of time. (*C*–*E*) CPRG-based bacterial competition assay. (*C*) Mixed cultures of *E. coli* expressing β-galactosidase and *X. citri* strains were grown on agar media supplemented with CPRG for 500 min at 25 °C, and absorbance at 572 nm was measured at 10-min intervals. (*D*) The instantaneous slope of the data shown in (*C*). (*E*) Histogram plotting the maximum slope values determined for each *X. citri* strain: WT, Δ*virB7* (ΔVirB7), and Δ7ΔXAC2609-GFP carrying the empty pBRA vector, the vector expressing X-Tfe^{XAC2609} (XAC2609), or the indicated mutants. Colors and symbols used for each *X. citri* strain in *C* and *D* are shown in *E*. Three to five independent experiments were performed for each strain. Error bars represent SD of the mean. CFU, colony forming unit.

images of Δ7Δ2609-GFP + X-Tfi^{XAC3633}/X-Tfe^{XAC3634} inducing contact-dependent lysis of *E. coli* cells.

Fig. 5*E* shows an alignment of the XVIPCD sequences of X-Tfe^{XAC3634} and X-Tfe^{XAC2609}, which share 45% sequence identity over 120 residues. We then investigated whether mutations in the XVIPCD of X-Tfe^{XAC3634} result in phenotypes similar to those observed for the corresponding mutations in X-Tfe^{XAC2609}. Fig. 5 *F* and *G* show the results of CPRG-based *E. coli* lysis assays for *X. citri* Δ7Δ2609-GFP cells containing plasmids coexpressing X-Tfi^{XAC3633} and wild-type or mutant versions of X-Tfe^{XAC3634}. The complemented Δ7Δ2609-GFP strain expressing the wild-type effector kills with an efficiency ∼87% of that of wild-type *X. citri* cells. The P597A mutation in X-Tfe^{XAC3634} produced no significant decrease in killing efficiency as observed for the corresponding P400A mutation in X-Tfe^{XAC2609}. The P514A/D515A and D560A mutations resulted in partial reductions in killing (46 and 51% of wild-type levels, respectively; Fig. 5 *F* and *G*), very similar to that observed for the equivalent X-Tfe^{XAC2609} H315A/P316A/D317A and D363A mutations, respectively. Two double mutations in X-Tfe^{XAC3634} (F572A/V574A and D580A/P581A) resulted in significant reductions in *E. coli* killing (11 and 10% of wild-type values), as was observed for the corresponding mutations in X-Tfe^{XAC2609} (F375A/V377A and D383A/P384A). Finally, when the last nine residues of X-Tfe^{XAC3634} (QRSQTRSVG) were deleted, no significant *E. coli* killing was observed, again pointing to an important role for the extreme carboxyl terminus of XVIPCDs in X-Tfe transfer to the target cell. The results obtained from the XAC2609$_{XVIPCD}$–VirD4$_{AAD}$ binding assays (ITC experiments in *SI Appendix*, Fig. S9) and the X-Tfe^{XAC2609}- and X-Tfe^{XAC3634}-dependent *E. coli* killing experiments (Figs. 4 and 5) are summarized and compared in *SI Appendix*, Fig. S12.

Discussion

The X-Tfe XVIPCD secretion signal can be divided into two general regions. The N-terminal ∼80 residues adopt an ααβββ fold and seem to be necessary and sufficient for interactions with the VirD4 AAD, since point mutations in highly conserved residues strongly diminish the stability of the complex. This well-folded domain is required but is not itself sufficient for substrate

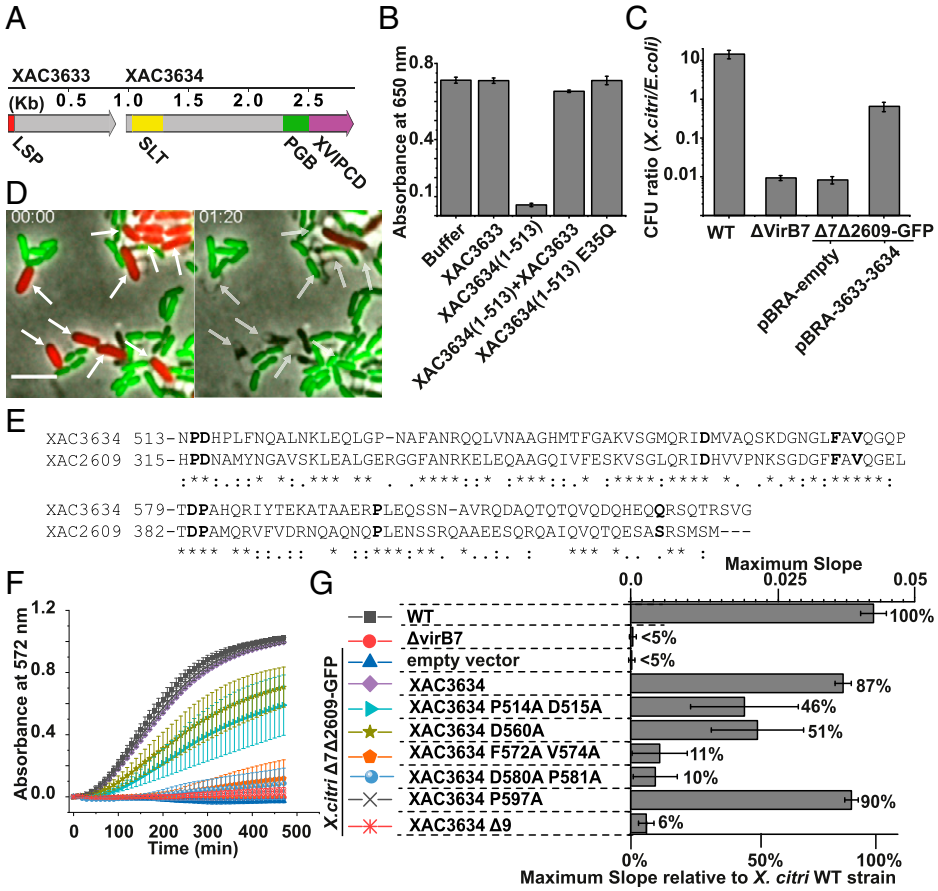

Fig. 5. XVIPCD features required for X-Tfe^{XAC3634} secretion. (*A*) Schematic of *X. citri* genomic region that encodes X-Tfi^{XAC3633} and X-Tfe^{XAC3634}. Predicted functional domains are shown: lipoprotein signal peptide (LSP) in X-Tfi^{XAC3633}; soluble lytic transglycosylase domain (SLT), peptidoglycan-binding domain (PGB), and the XVIPCD in X-Tfe^{XAC3634}. (*B*) Peptidoglycan hydrolysis assay. Absorbance at 650 nm of *M. luteus* cell wall suspensions treated with buffer or with purified His-tagged X-Tfi$^{XAC3633}{}_{(40–300)}$, X-Tfe$^{XAC3634}{}_{(1–513)}$, X-Tfe$^{XAC3634}{}_{(1–513)}$–X-Tfi$^{XAC3633}{}_{(40–300)}$, and X-Tfe$^{XAC3634}{}_{(1–513)}$E35Q. (*C*) The ratio of the number of viable *X. citri* and *E. coli* RFP cells after 36 h of interbacterial competition during coculture on LB agar. *X. citri* strains used: WT, Δ*virB7*, and Δ7ΔXAC2609-GFP carrying the empty pBRA vector or the pBRA vector expressing the X-Tfi^{XAC3633}–X-Tfe^{XAC3634} bicistronic operon. Error bars represent the SD of three experiments. (*D*) Time-lapse microscopy showing *X. citri* Δ7ΔXAC2609-GFP carrying pBRA-XAC3633-XAC3634 (green) in coculture with *E. coli* RFP (red). White and semitransparent arrows point to *E. coli* cells before and after lysis. Time points are in minutes. (Scale bar: 5 μm.) See also Movie S3. (*E*) Pairwise sequence alignment of the XVIPCD domains of X-Tfe^{XAC2609} (XAC2609) and X-Tfe^{XAC3634} (XAC3634). Mutated residues in bold. (*F*) CPRG bacterial competition assay (conditions as in Fig. 4*C*). (*G*) Histogram plotting the maximum slope values determined for each *X. citri* strain: WT, Δ*virB7*, and Δ7ΔXAC2609-GFP carrying the empty pBRA vector, the vector expressing the bicistronic X-Tfi^{XAC3633}–X-Tfe^{XAC3634} operon, or the indicated mutants in X-Tfe^{XAC3634}. Colors and symbols used for each *X. citri* strain in *F* are indicated in *G*. Three to five independent experiments were performed for each strain. Error bars show SD of the mean.

translocation. One interesting feature of this region is its sensitivity to pH. At slightly basic pH 8.0, which most closely mimics the conditions in the bacterial cytosol (30–32), its structure is relatively stable, which may be necessary for its interaction with VirD4. However, at more acidic pHs, which may correspond to conditions in the periplasm, the ααβββ region seems to become at least partially unfolded. In a manner analogous to the observation that the TrwC relaxase needs to be unfolded to pass through the conjugative R388 T4SS (44), the pH-dependent instability of the XVIPCD may facilitate its unfolding and translocation through the periplasmic portion of the X-T4SS channel.

Efficient X-Tfe translocation into the target cell requires a carboxyl-terminal tail portion of the XVIPCD that varies in length among X-Tfes and has no discernable sequence motifs, except for a high glutamine content in its N-terminal portion and a mixed hydrophobic and positively charged extreme carboxyl terminus. Interestingly, while deletion of the last 20 or last 6 residues in X-Tfe^{XAC2609} or the last nine residues in X-Tfe^{XAC3634} abolished their translocation, mutating the last nine glutamines to alanine in X-Tfe^{XAC2609} (from positions 397–431) did not significantly affect X-Tfe^{XAC2609} translocation into target cells. Therefore, the precise function of the glutamine residues in XVIPCDs remains enigmatic. It may be that the glutamines favor the formation of a specific structure during translocation or that they participate in an unknown protein–protein interaction that is not disrupted by their mutation to alanines.

Type IV secretion systems employ a T4CP or type IV coupling complex (T4CC) for initial substrate recognition, and the translocation signals recognized by them are very diverse (45). Recognition can involve direct interactions with the VirD4 AAD, as is the case for *A. tumefaciens* VirD2, *E. faecalis* pCF10 PcfF (26), and *X. citri* X-Tfes, or may require the participation of adaptor proteins and/or VirD4 C-terminal extensions, as is the case for *Legionella pneumophila* (38, 39) and F-family plasmids (40, 46). It is therefore relevant to ask whether X-Tfe XVIPCDs share common structural or sequence features with the secretion signals of other T4SS substrates.

Ubiquitous substrates of T4SSs are the relaxases that recognize, nick, and form covalent conjugates at specific DNA sequences of mobilizable elements (usually plasmids). The

bifunctional TraI relaxase of F and related plasmids contains two homologous internal translocation signal domains (TSA and TSB), plus a carboxyl-terminal domain that binds to the tetrameric adapter protein TraM, which in turn binds to a carboxyl-terminal extension of the T4CP TraD (40, 47–50). None of these domains present topological similarity with $XAC2609_{XVIPCD}\Delta20$ (40, 47, 51, 52).

In *Bartonella* species, relaxases involved in plasmid transfer as well as *Bartonella* effector proteins (BEPS) have one or more carboxyl-terminal BID (Bep intracellular delivery) domains that are thought to be necessary for recognition by the T4CP (53, 54). The four-helix bundle topology observed for BID domains (53) is structurally distinct from that of the XVIPCD. However, these BID domains are followed by a disordered, positively charged carboxyl-terminal tail, the deletion of which was shown to almost completely abolish translocation of one effector, BepD (55), an intriguing parallel with our observations of the effects of carboxyl-terminal deletions in X-$Tfe^{XAC2609}$ and X-$Tfe^{XAC3634}$. Similarly, in *A. tumefaciens*, the transport signal for T4SS protein substrates has been shown to include a structurally disordered hydrophilic and positively charged carboxyl terminus. Vergunst et al. (56) tested specific characteristics of the transport signal in one *A. tumefaciens* T4SS substrate, VirF, and found that deletion of any one of several positively charged arginine residues resulted in severe reductions in translocation efficiency. Also, deletion of one, two, or three of the last residues (Arg, Gly, Leu) abolished VirF transfer.

In the case of the much larger and structurally elaborate *Legionella* Dot/Icm T4SS that secretes several hundred effectors, substrate recognition is mediated by a large T4CC that is thought to contain six copies of a DotLMNXY pentamer plus the IcmSW chaperone (38, 57). Here, the VirD4 homolog DotL has a large carboxyl-terminal extension that interacts with many other components, and substrates are recognized and prepared for secretion via IcmSW-dependent and IcmSW-independent mechanisms (38, 39, 57, 58–62). The crystal structure of the VpdB–LvgA effector–adapter complex bound to IcmSW–DotL–DotN has been solved, but none of the components have topologies similar to that of the X-$Tfe^{XAC2609}$ XVIPCD. Among Icm-independent substrates, some contain a carboxyl-terminal glutamate-rich signal peptide (Glu-rich SP) that interacts with the T4CC subunit DotM (38, 63). Interestingly, the last 20 residues of this Glu-rich SP can be divided into two regions: a Glu-rich acidic region between positions −20 to −8, which transitions into a positively charged region between positions −7 and −1 that is also rich in serine and hydrophobic residues (63), a pattern somewhat similar to what we observe for the carboxyl-terminal tail of XVIPCDs (Fig. 2*B*). Another *L. pneumophila* IcmSW-independent effector, RalF, lacks a Glu-rich SP but rather requires a hydrophobic residue at the third position before the carboxyl terminus for translocation, while changing a neighboring positively charged lysine to alanine or to a negatively charged glutamate residue had relatively little effect (64).

We can conclude that the folded αααβββ N-terminal region of the XVIPCD is structurally distinct from previously described secretion signals of T4SS substrates or adapter proteins from other organisms. Conserved residues that map to the surface of the three-stranded beta sheet and its associated loops are strong candidates for directly participating in its interactions with VirD4. In addition to this folded module, efficient X-Tfe translocation into the target cell requires an intact carboxyl-terminal tail portion of the XVIPCD. This region seems to share some general features with the secretion signals found in the substrates of some other T4SSs. Here, what seems to be important are the physical properties of the carboxyl terminus rather than any specific sequence.

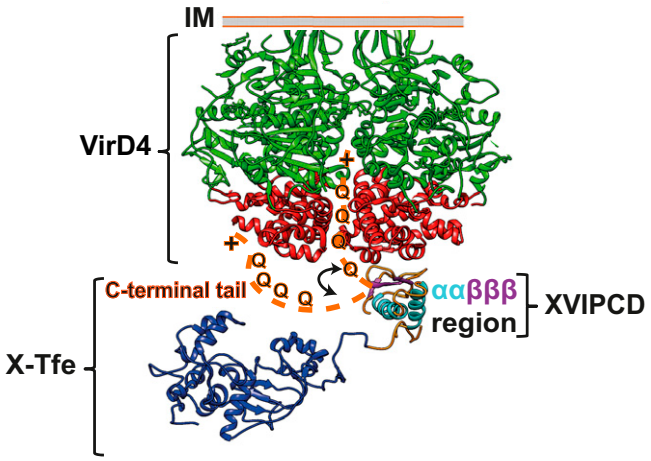

Fig. 6. Schematic of the association of an X-Tfe with VirD4. The model of the VirD4 hexamer is based on the TrwB structure (PDB code: 1GKI (27), with AADs colored red and the rest of the protein colored green. Below is shown a composite model of X-$Tfe^{XAC2609}$, in which the region containing the GH19 and PGBs [residues 1–311; blue; modeled based on the crystal structure of SltB3 from *P. aeruginosa* (PDB ID 5ANZ; 66)] is followed by the XVIPCD (residues 315–431), which is divided into the αααβββ region and the unstructured carboxyl-terminal tail (orange dotted line) containing glutamine-rich (Q) and hydrophobic/positively charged zones (+). IM, inner membrane.

The previous considerations point to a separation of function for the structured and more conserved N-terminal and the unstructured and more variable carboxyl-terminal regions of the XVIPCD; the former directs the initial docking of the effector with the coupling protein, while the latter is necessary for an essential though as yet unknown step in the secretion process, as depicted in Fig. 6. This step could be related to effector recognition by unidentified adapter proteins before binding to VirD4 or at some stage subsequent to VirD4 binding such as activating ATPase activity or initiating the threading of the unfolded polypeptide chain through the inner membrane, periplasmatic, and/or outer membrane complexes of the T4SS channel.

Materials and Methods

Detailed procedures and sources of reagents are described in *SI Appendix*.

SAXS. SAXS experiments were carried out at the SAXS 2 beamline of the Brazilian Synchrotron Light Laboratory using 1.55-Å radiation and a sample to detector distance of 935.5 mm.

NMR Spectroscopy and Structure Calculation. NMR experiments were performed on a Bruker Avance III 800 MHz NMR spectrometer at 25 °C equipped with a TCI cryogenic probe. All NMR samples consisted of ^{15}N-labeled or ^{15}N and ^{13}C doubly labeled $XAC2609_{XVIPCD}\Delta20$ at a concentration of 1.6 mM in NMR buffer [20 mM Tris·HCl (pH 8), 100 mM NaCl, 0.1% glycerol, 7% D_2O, 0.05% sodium azide] unless otherwise stated. Backbone resonance assignments were obtained for most residues, except for 318–319, 333, 340, 369–370, 381–382, 397–399, and 403–408. These assignments were obtained from the analysis of a set of triple-resonance NMR experiments implemented using NMRLib (65). Side-chain resonances were obtained from the analysis of 3D (H)CCH (TOCSY) and 3D H(C)CH-TOCSY (total correlation spectroscopy) experiments using nonuniform sampling (66, 67). All NOE spectroscopy (NOESY) experiments were recorded using a mixing time of 100 ms. The following NOE experiments were recorded in H_2O: 3D ^{15}N NOESY-HSQC, ^{13}C NOESY-HSQC, and ^{1}H-^{1}H 2D NOESY. NOEs from aromatic residues were obtained from the analysis of a ^{13}C NOESY-HSQC experiment recorded as a 2D plane and with the ^{13}C carrier frequency centered in the aromatic region. Additionally, H(C)CH-TOCSY, (H)CCH-TOCSY, ^{13}C NOESY-HSQC, ^{15}N NOESY-HSQC, and 2D NOE spectra were collected using a lyophilized sample resuspended in deuterated buffer. The NMR titration was carried out by recording ^{1}H-^{15}N-HSQC experiments of ^{15}N-^{13}C-$XAC2609_{XVIPCD}\Delta20$ at a concentration of

160 μM in the absence or presence of $VirD4_{AAD}$ at 40, 80, 120, 160, and 320 μM protein concentrations. Ratios of the ^{1}H-^{15}N-HSQC peak heights at the last titration point [$XAC2609_{XVIPCD}\Delta20$ (160 μM):$VirD4_{AAD}$ (320 μM)] with respect to the first titration point [$XAC2609_{XVIPCD}\Delta20$ (160 μM)] were mapped on the NMR structure of $XAC2609_{XVIPCD}\Delta20$. NMR spectra were processed with NMRPipe (68) and analyzed with CcpNmr Analysis (69); data analysis and graphs were made using Origin (2020). Automated NOE assignment and structure calculation were performed with the Ariaweb server at https://ariaweb.pasteur.fr/login?next=/ (70) by simulated annealing molecular dynamics in torsion angle space (71), based on the assignments for 81.9% of backbone resonances and 73.8% of ^{1}H side-chain resonances, 5,462 manually picked NOESY cross-peaks, and 154 dihedral angle restraints obtained using TALOS-N (33). The precision of the final ensemble is 0.69 Å for the backbone coordinates within residues 316–393. (Table S3).

CPRG Bacteria-Killing Experiments. CPRG bacteria-killing assays were performed as previously described (22), with some adaptations. The 5-μL mixtures of *X. citri* strains (optical density at 600 nm [OD_{600nm}] = 0.5) and *E. coli* MG1655 cells (OD_{600nm} = 5) were spotted over wells filled with agarose-CPRG medium using 96-well plates. Absorbance was monitored at 572 nm (A_{572nm}) at 10-min intervals for 8 h. Normalization was performed by dividing absorbance values at each time point by the A_{572nm} at 480 min. Data reduction, first derivative determination, and statistical analysis was performed using Origin.

Data Availability. NMR data and model ensemble have been deposited in the Biological Magnetic Resonance Data Bank (BMRB) (code 30908) (73) and Protein Data Bank (PDB) (code 7MU9) (74). All other data are available in the main text or the *SI Appendix*.

ACKNOWLEDGMENTS. We thank Dr. Peter Christie for the plasmid constructs used to express VirD2, PcfF, and PcfG and we thank Dr. Frederico Gueiros Filho for fluorescence microscopy access. We acknowledge financial support from Fundação de Amparo à Pesquisa do Estado de São Paulo (2017/17303-7, 2018/09277-9, 2015/18237-2, and 2016/00458-5).

1. D. Ghosal *et al.*, Molecular architecture, polar targeting and biogenesis of the Legionella Dot/Icm T4SS. *Nat. Microbiol.* **4**, 1173–1182 (2019).
2. J. M. Chung *et al.*, Structure of the *Helicobacter pylori* Cag type IV secretion system. *eLife* **8**, e47644 (2019).
3. H. Hilbi, H. Nagai, T. Kubori, C. R. Roy, Subversion of host membrane dynamics by the Legionella Dot/Icm type IV secretion system. *Curr. Top. Microbiol. Immunol.* **413**, 221–242 (2017).
4. Y. Ke, Y. Wang, W. Li, Z. Chen, Type IV secretion system of Brucella spp. and its effectors. *Front. Cell. Infect. Microbiol.* **5**, 72 (2015).
5. A. C. Vergunst *et al.*, VirB/D4-dependent protein translocation from Agrobacterium into plant cells. *Science* **290**, 979–982 (2000).
6. J. E. Gordon, P. J. Christie, The Agrobacterium Ti plasmids. *Microbiol. Spectr.* **2**, 10.1128/microbiolspec.PLAS-0010-2013 (2014).
7. A. Ilangovan, S. Connery, G. Waksman, Structural biology of the Gram-negative bacterial conjugation systems. *Trends Microbiol.* **23**, 301–310 (2015).
8. F. de la Cruz, J. Davies, Horizontal gene transfer and the origin of species: Lessons from bacteria. *Trends Microbiol.* **8**, 128–133 (2000).
9. R. A. F. Wozniak, M. K. Waldor, Integrative and conjugative elements: Mosaic mobile genetic elements enabling dynamic lateral gene flow. *Nat. Rev. Microbiol.* **8**, 552–563 (2010).
10. C. M. Johnson, A. D. Grossman, Integrative and conjugative elements (ICEs): What They do and how they work. *Annu. Rev. Genet.* **49**, 577–601 (2015).
11. D. Arutyunov, L. S. Frost, F conjugation: Back to the beginning. *Plasmid* **70**, 18–32 (2013).
12. T. R. D. Costa *et al.*, Structure of the bacterial sex F pilus reveals an assembly of a stoichiometric protein-phospholipid complex. *Cell* **166**, 1436–1444.e10 (2016).
13. D. P. Souza *et al.*, Bacterial killing via a type IV secretion system. *Nat. Commun.* **6**, 6453 (2015).
14. G. G. Sgro *et al.*, Bacteria-killing type IV secretion systems. *Front. Microbiol.* **10**, 1078 (2019).
15. E. Bayer-Santos *et al.*, The opportunistic pathogen *Stenotrophomonas maltophilia* utilizes a type IV secretion system for interbacterial killing. *PLoS Pathog.* **15**, e1007651 (2019).
16. L. C. Oliveira *et al.*, VirB7 and VirB9 interactions are required for the assembly and antibacterial activity of a type IV secretion system. *Structure* **24**, 1707–1718 (2016).
17. H. H. Low *et al.*, Structure of a type IV secretion system. *Nature* **508**, 550–553 (2014).
18. A. Redzej *et al.*, Structure of a VirD4 coupling protein bound to a VirB type IV secretion machinery. *EMBO J.* **36**, 3080–3095 (2017).
19. E. Grohmann, P. J. Christie, G. Waksman, S. Backert, Type IV secretion in Gram-negative and Gram-positive bacteria. *Mol. Microbiol.* **107**, 455–471 (2018).
20. C. E. Alvarez-Martinez, P. J. Christie, Biological diversity of prokaryotic type IV secretion systems. *Microbiol. Mol. Biol. Rev.* **73**, 775–808 (2009).
21. G. Waksman, From conjugation to T4S systems in Gram-negative bacteria: A mechanistic biology perspective. *EMBO Rep.* **20**, e47012 (2019).
22. G. G. Sgro *et al.*, Cryo-EM structure of the bacteria-killing type IV secretion system core complex from *Xanthomonas citri*. *Nat. Microbiol.* **3**, 1429–1440 (2018).
23. W. Cenens *et al.*, Bactericidal type IV secretion system homeostasis in *Xanthomonas citri*. *PLoS Pathog.* **16**, e1008561 (2020).
24. D. P. Souza *et al.*, A component of the Xanthomonadaceae type IV secretion system combines a VirB7 motif with a N0 domain found in outer membrane transport proteins. *PLoS Pathog.* **7**, e1002031 (2011).
25. M. C. Alegria *et al.*, Identification of new protein-protein interactions involving the products of the chromosome- and plasmid-encoded type IV secretion loci of the phytopathogen *Xanthomonas axonopodis* pv. citri. *J. Bacteriol.* **187**, 2315–2325 (2005).
26. N. Whitaker *et al.*, The all-alpha domains of coupling proteins from the *Agrobacterium tumefaciens* VirB/VirD4 and *Enterococcus faecalis* pCF10-encoded type IV secretion systems confer specificity to binding of cognate DNA substrates. *J. Bacteriol.* **197**, 2335–2349 (2015).
27. F. X. Gomis-Rüth *et al.*, The bacterial conjugation protein TrwB resembles ring helicases and F1-ATPase. *Nature* **409**, 637–641 (2001).
28. H. D. T. Mertens, D. I. Svergun, Structural characterization of proteins and complexes using small-angle X-ray solution scattering. *J. Struct. Biol.* **172**, 128–141 (2010).
29. M. C. Alegria *et al.*, New protein-protein interactions identified for the regulatory and structural components and substrates of the type III Secretion system of the phytopathogen *Xanthomonas axonopodis* Pathovar citri. *J. Bacteriol.* **186**, 6186–6197 (2004).
30. J. C. Wilks, J. L. Slonczewski, pH of the cytoplasm and periplasm of *Escherichia coli*: Rapid measurement by green fluorescent protein fluorimetry. *J. Bacteriol.* **189**, 5601–5607 (2007).
31. J. L. Slonczewski, B. P. Rosen, J. R. Alger, R. M. Macnab, pH homeostasis in *Escherichia coli*: Measurement by 31P nuclear magnetic resonance of methylphosphonate and phosphate. *Proc. Natl. Acad. Sci. U.S.A.* **78**, 6271–6275 (1981).
32. E. Padan, E. Bibi, M. Ito, T. A. Krulwich, Alkaline pH homeostasis in bacteria: New insights. *Biochim. Biophys. Acta* **1717**, 67–88 (2005).
33. Y. Shen, A. Bax, Protein backbone and sidechain torsion angles predicted from NMR chemical shifts using artificial neural networks. *J. Biomol. NMR* **56**, 227–241 (2013).
34. L. Holm, Using Dali for protein structure comparison. *Methods Mol. Biol.* **2112**, 29–42 (2020).
35. T. S. Kumarevel *et al.*, Crystal structure of HutP, an RNA binding antitermination protein. RCSB. https://www.rcsb.org/structure/1VEA. Accessed 1 December 2020.
36. M. Källberg *et al.*, Template-based protein structure modeling using the RaptorX web server. *Nat. Protoc.* **7**, 1511–1522 (2012).
37. S. Wang, S. Sun, Z. Li, R. Zhang, J. Xu, Accurate de novo prediction of protein contact map by ultra-deep learning model. *PLOS Comput. Biol.* **13**, e1005324 (2017).
38. A. Meir *et al.*, Mechanism of effector capture and delivery by the type IV secretion system from Legionella pneumophila. *Nat. Commun.* **11**, 2864 (2020).
39. H. Kim *et al.*, Structural basis for effector protein recognition by the Dot/Icm Type IVB coupling protein complex. *Nat. Commun.* **11**, 2623 (2020).
40. J. Lu *et al.*, Structural basis of specific TraD-TraM recognition during F plasmid-mediated bacterial conjugation. *Mol. Microbiol.* **70**, 89–99 (2008).
41. A. Marchler-Bauer *et al.*, CDD: A Conserved Domain Database for the functional annotation of proteins. *Nucleic Acids Res.* **39**, D225–D229 (2011).
42. E. Scheurwater, C. W. Reid, A. J. Clarke, Lytic transglycosylases: Bacterial space-making autolysins. *Int. J. Biochem. Cell Biol.* **40**, 586–591 (2008).
43. D. A. Dik, D. R. Marous, J. F. Fisher, S. Mobashery, Lytic transglycosylases: Concinnity in concision of the bacterial cell wall. *Crit. Rev. Biochem. Mol. Biol.* **52**, 503–542 (2017).
44. M. Trokter, G. Waksman, Translocation through the conjugative type IV secretion system requires unfolding of its protein substrate. *J. Bacteriol.* **200**, e00615-17 (2018).
45. M. Llosa, I. Alkorta, Coupling proteins in type IV secretion. *Curr. Top. Microbiol. Immunol.* **413**, 143–168 (2017).
46. C. Disqué-Kochem, B. Dreiseikelmann, The cytoplasmic DNA-binding protein TraM binds to the inner membrane protein TraD in vitro. *J. Bacteriol.* **179**, 6133–6137 (1997).
47. A. Redzej *et al.*, Structure of a translocation signal domain mediating conjugative transfer by type IV secretion systems. *Mol. Microbiol.* **89**, 324–333 (2013).
48. E. L. Zechner, G. Moncalián, F. de la Cruz, Relaxases and plasmid transfer in gram-negative bacteria. *Curr. Top. Microbiol. Immunol.* **413**, 93–113 (2017).
49. H. Ragonese, D. Haisch, E. Villareal, J. H. Choi, S. W. Matson, The F plasmid-encoded TraM protein stimulates relaxosome-mediated cleavage at oriT through an interaction with TraI. *Mol. Microbiol.* **63**, 1173–1184 (2007).
50. S. Lang *et al.*, Molecular recognition determinants for type IV secretion of diverse families of conjugative relaxases. *Mol. Microbiol.* **78**, 1539–1555 (2010).
51. A. Ilangovan *et al.*, Cryo-EM structure of a relaxase reveals the molecular basis of DNA unwinding during bacterial conjugation. *Cell* **169**, 708–721.e12 (2017).
52. L. M. Guogas, S. A. Kennedy, J.-H. Lee, M. R. Redinbo, A novel fold in the TraI relaxase-helicase c-terminal domain is essential for conjugative DNA transfer. *J. Mol. Biol.* **386**, 554–568 (2009).
53. F. V. Stanger *et al.*, The BID domain of type IV secretion substrates forms a conserved four-helix bundle topped with a hook. *Structure* **25**, 203–211 (2017).

54. G. Schröder, R. Schuelein, M. Quebatte, C. Dehio, Conjugative DNA transfer into human cells by the VirB/VirD4 type IV secretion system of the bacterial pathogen *Bartonella henselae*. *Proc. Natl. Acad. Sci. U.S.A.* **108**, 14643–14648 (2011).
55. R. Schulein *et al.*, A bipartite signal mediates the transfer of type IV secretion substrates of *Bartonella henselae* into human cells. *Proc. Natl. Acad. Sci. U.S.A.* **102**, 856–861 (2005).
56. A. C. Vergunst *et al.*, Positive charge is an important feature of the C-terminal transport signal of the VirB/D4-translocated proteins of Agrobacterium. *Proc. Natl. Acad. Sci. U.S.A.* **102**, 832–837 (2005).
57. M. C. Sutherland, T. L. Nguyen, V. Tseng, J. P. Vogel, The Legionella IcmSW complex directly interacts with DotL to mediate translocation of adaptor-dependent substrates. *PLoS Pathog.* **8**, e1002910 (2012).
58. M.-J. Kwak *et al*., Architecture of the type IV coupling protein complex of *Legionella pneumophila*. *Nat. Microbiol.* **2**, 17114 (2017).
59. S. Ninio, D. M. Zuckman-Cholon, E. D. Cambronne, C. R. Roy, The Legionella IcmS-IcmW protein complex is important for Dot/Icm-mediated protein translocation. *Mol. Microbiol.* **55**, 912–926 (2005).
60. J. P. Bardill, J. L. Miller, J. P. Vogel, IcmS-dependent translocation of SdeA into macrophages by the *Legionella pneumophila* type IV secretion system. *Mol. Microbiol.* **56**, 90–103 (2005).
61. E. D. Cambronne, C. R. Roy, The *Legionella pneumophila* IcmSW complex interacts with multiple Dot/Icm effectors to facilitate type IV translocation. *PLoS Pathog.* **3**, e188 (2007).
62. F. Habyarimana, C. T. Price, M. Santic, S. Al-Khodor, Y. A. Kwaik, Molecular characterization of the Dot/Icm-translocated AnkH and AnkJ eukaryotic-like effectors of *Legionella pneumophila*. *Infect. Immun.* **78**, 1123–1134 (2010).
63. Z. Lifshitz *et al.*, Computational modeling and experimental validation of the Legionella and Coxiella virulence-related type-IVB secretion signal. *Proc. Natl. Acad. Sci. U.S.A.* **110**, E707–E715 (2013).
64. H. Nagai *et al.*, A C-terminal translocation signal required for Dot/Icm-dependent delivery of the Legionella RalF protein to host cells. *Proc. Natl. Acad. Sci. U.S.A.* **102**, 826–831 (2005).
65. A. Favier, B. Brutscher, NMRlib: User-friendly pulse sequence tools for Bruker NMR spectrometers. *J. Biomol. NMR* **73**, 199–211 (2019).
66. V. Y. Orekhov, V. A. Jaravine, Analysis of non-uniformly sampled spectra with multi-dimensional decomposition. *Prog. Nucl. Magn. Reson. Spectrosc.* **59**, 271–292 (2011).
67. S. G. Hyberts, A. G. Milbradt, A. B. Wagner, H. Arthanari, G. Wagner, Application of iterative soft thresholding for fast reconstruction of NMR data non-uniformly sampled with multidimensional Poisson Gap scheduling. *J. Biomol. NMR* **52**, 315–327 (2012).
68. F. Delaglio *et al.*, NMRPipe: A multidimensional spectral processing system based on UNIX pipes. *J. Biomol. NMR* **6**, 277–293 (1995).
69. W. F. Vranken *et al.*, The CCPN data model for NMR spectroscopy: Development of a software pipeline. *Proteins* **59**, 687–696 (2005).
70. F. Allain, F. Mareuil, H. Ménager, M. Nilges, B. Bardiaux, ARIAweb: A server for automated NMR structure calculation. *Nucleic Acids Res.* **48** (W1), W41–W47 (2020).
71. A. T. Brünger *et al.*, Crystallography & NMR system: A new software suite for macromolecular structure determination. *Acta Crystallogr. D Biol. Crystallogr.* **54**, 905–921 (1998).
72. NCBI Resource Coordinators, Database resources of the National Center for Biotechnology Information. *Nucleic Acids Res.* **46** (D1), D8–D13 (2018).
73. G. U. Oka, R. K. Salinas, C. S. Farah, Solution NMR structure of the XVIPCD region from the T4SS effector X-Tfe(XAC2609) from Xanthomonas citri. Biological Magnetic Resonance Data Bank. https://bmrb.io/data_library/summary/index.php?bmrbId=30908. Deposited 17 May 2021.
74. G. U. Oka, R. K. Salinas, C. S. Farah, Solution NMR structure of the XVIPCD region from the T4SS effector X-Tfe(XAC2609) from Xanthomonas citri. Protein Data Bank. https://www.rcsb.org/structure/7MU9. Deposited 17 May 2021.